

Immobilizing Pd nanoparticles on amine-functionalized yolk-shell mesoporous silica nanospheres for efficient H₂ production from formic acid dehydrogenation

Chunhui Zhou ^a, Song Li ^a, Hao Chai ^a, Quan Liu ^a, Jinsong Hu ^{a,*}, Zhentao Liu ^b, Ke Yu ^b, Fei Fan ^c, Wenwu Zhou ^c, Aijun Duan ^b, Chunming Xu ^b, Xilong Wang ^{b,*}

^a Analytical and Testing Center, School of Chemical Engineering, Anhui University of Science and Technology, Huainan 232001, China

^b State Key Laboratory of Heavy Oil Processing, College of Chemical Engineering and Environment, China University of Petroleum, Beijing 102249, China

^c College of Chemistry and Chemical Engineering, Xi'an University of Science and Technology, Xi'an 710054, China



ARTICLE INFO

Keywords:
Yolk-shell mesoporous silica nanospheres
NH₂-functionalization
Pd nanoparticles
Formic acid
H₂ production

ABSTRACT

Ultrafine Pd nanoparticles (NPs), immobilized within amine-functionalized yolk-shell mesoporous silica nanospheres (YSMSNs), have been elaborately prepared to facilitate the highly effective formic acid (FA) dehydrogenation. The optimized Pd/YSMSNs-NH₂(10–3, 10 wt% Pd loading and 3 mL of amine treatment on YSMSNs), displays the extraordinary turnover frequency (TOF, 9108 h⁻¹) and stability at 343 K, achieving 100% FA conversion and H₂ selectivity, which is higher than other documented heterogeneous catalysts. The radially oriented pore channels can facilitate the mass transfer of reactants. The amine groups on the YSMSNs-NH₂ effectively promote the cleavage of the O-H bond within FA. Furthermore, the ultrafine size of the Pd NPs and their high dispersion on the YSMSNs-NH₂ provide a wealth of active sites for catalysis. Lastly, the metal-support interaction (MSI) between the Pd NPs and YSMSNs-NH₂ further enhances the catalytic performance. This work provides a new strategy into developing effective silica-based heterogeneous catalysts for FA dehydrogenation.

1. Introduction

H₂ emerges as a promising energy source, owing to its renewable nature, substantial mass-energy density, and zero-carbon emission characteristics. Therefore, the H₂ fuel cell is regarded as a leading candidate for an ultimate energy solution [1]. However, the storage and transportation issues of H₂ on an industrial scale are still the big challenges [2–5]. To solve this troublesome problem, liquid organic hydrogen carriers (LOHCs) are extensively employed as hydrogen-rich substances for the purpose of storing and releasing H₂ under moderate conditions in conjunction with appropriate catalysts [6–10]. Within the scope of the current research into diverse LOHCs, FA emerges as an exceptional H₂ carrier due to several key attributes. These include a notable high mass density and volumetric capacity, quantified at 4.4 wt % and 53.4 g/L, respectively. Moreover, FA exhibits low toxicity and flammability, and the presence of the suitable melting and boiling points that render it amenable to facile storage and transport under ambient conditions [11–13]. Moreover, it is noteworthy that FA represents a well-established liquid byproduct of the biomass conversion process and

carbon dioxide (CO₂) reduction, thereby reflecting its wide-ranging origins [11–18].

Specifically, FA decomposition exhibits dual reaction pathways. The first involves FA dehydrogenation, resulting in the generation of H₂ and CO₂, while the second pathway entails a dehydration process that yields water (H₂O) and carbon monoxide (CO) [19]. Evidently, the utilization of the CO-free reaction pathway is prioritized within the context of H₂ fuel cells, as the presence of CO generated during the dehydration process has the potential to detrimentally impact metal catalysts by means of catalytic poisoning. Hence, it is imperative to design catalysts with the capacity to finely modulate the selectivity of FA dehydrogenation, ultimately achieving complete H₂ generation [20]. Intensive investigations have been conducted on homogeneous catalysts for FA dehydrogenation due to their remarkable activity and selectivity. Nevertheless, the feasibility of these homogeneous systems for practical applications is hampered by their inherent challenges, notably low stability, limited reusability, and the elevated costs associated with both the metal and ligand components [14,21,22]. Heterogeneous catalysts employed in FA dehydrogenation offer a notably promising prospect,

* Corresponding authors.

E-mail addresses: jshu@aust.edu.cn (J. Hu), wxl@cup.edu.cn (X. Wang).

primarily attributable to their robust stability, reusability, and the comparative cost-effectiveness of the catalytic materials [13,23,24]. At present, Pd-based catalysts have emerged as the foremost candidates among heterogeneous catalysts for FA dehydrogenation, owing to their commendable catalytic activity and robust stability [24–34].

In addition to the judicious choice of active metal sites for FA dehydrogenation, the selection of catalyst supports assumes a pivotal role in shaping the resulting catalysts. This is attributed to its profound influence on critical factors such as size and distribution of active metal species, the MSI, and the distinctive pore structures of the supports, which facilitate the rapid transfer of reactants [13,35]. Various support materials, encompassing silica, carbon-based substances, metal oxides, metal-organic frameworks (MOFs), and MOFs-derived materials, have garnered extensive attention in the FA dehydrogenation [23,24]. Extensive research has been devoted to silica supports, driven by their remarkable attributes, including elevated thermal and chemical stabilities, well-defined specific surface area, and the capability to fine-tune pore structures [36,37]. Furthermore, the silanol groups (Si-OH) on the surface can be readily functionalized with amine moieties, serving as interaction sites for the formation of ultrafine metal NPs or nanoclusters (NCS) upon the introduction of active metals. These amine-functionalized sites also play a pivotal role as proton scavengers, thereby promoting the cleavage of the O-H bond in FA [38–47]. However, there are limited examples of silica-supported monometallic Pd NPs systems. In a recent study by Lee et al., Pd NPs were successfully incorporated into a 3D-interconnected mesoporous silica matrix, specifically NH₂-KIE-6. The resultant catalyst, denoted as Pd-NH₂-KIE-6, showcased remarkable catalytic efficacy, achieving an initial TOF of 764 h⁻¹ within the first 10 min of reaction at room temperature [48]. Ahn and coworkers addressed the Pd NPs immobilized on the amine-functionalized fibrous silica KCC-1, and the resulting Pd/KCC-1-NH₂ displayed a good catalytic performance, giving a TOF of 332 h⁻¹ at 323 K in the first 20% conversion of FA [49]. Although the silica-supported monometallic Pd catalytic systems already showed the great potential in the FA dehydrogenation, their related catalytic activities need to be further improved, and developing more effective silica-based support is essential to realize the FA dehydrogenation on a large scale.

It was conceived that the YSMSNs, with radially oriented mesoporous channels, good hydrothermal stability, large pore volume, high porosity and surface area, adjustable yolk size and shell thickness that could improve the catalytic activity of Pd NPs for the dehydrogenation of FA [50–53]. Moreover, the silanol groups present on pristine YSMSNs can be easily functionalized with -NH₂ moieties. This modification offers a favorable prospect for anchoring active metals, preventing their aggregation into larger NPs. Consequently, it renders YSMSNs a promising support material for use in the context of FA dehydrogenation [40,44,45]. Until now, the YSMSNs as the support in the FA dehydrogenation application has not been reported, giving the huge potential in this research area because of the advantages of the structural properties of YSMSNs.

Herein, a series of ultrafine Pd NPs is immobilized on the amine-functionalized YSMSNs (YSMSNs-NH₂) successfully, which are prepared by the surface amine -functionalization and wet chemical co-reduction approaches. The influence of amine group content and Pd loading amount are studied systematically. The optimized catalyst, denoted as Pd/YSMSNs-NH₂(10–3), reveals extraordinary catalytic performance and a commendable level of stability in the FA dehydrogenation. Notably, it achieves an initial TOF (FA conversion reaches 20%) of 9108 h⁻¹ at 343 K, with the incorporation of sodium formate (SF) as an additive, ultimately achieving 100% FA conversion and H₂ selectivity for the whole catalytic process. Additionally, the optimized Pd/YSMSNs-NH₂(10–3) catalyst displays excellent stability with no significant decline in catalytic activity even after six runs, showcasing the practical application of efficient FA dehydrogenation catalysts.

2. Experimental section

2.1. Synthesis of the YSMSNs-NH₂

Firstly, the YSMSNs were prepared by a sol-gel method in ethanol solution according to the previous reports[52]. The detailed synthetic procedure could be found in the supporting information (SI). Then, the YSMSNs-NH₂ were prepared via a grafting method of YSMSNs with APTES according to the reports with minor changes[40,44,47]. Typically, for the 3 mL of amine reagent chemical treatment on YSMSNs to produce the YSMSNs-NH₂ as the example. Firstly, 500 mg YSMSNs were put into an oven at 105 °C overnight before surface functionalization, then 30 mL of anhydrous toluene was added into the YSMSNs, then 3 mL of APTES was added to the above-mixed solution. The mixture above was stirred vigorously at 80 °C for 24 h. Afterwards, the reaction mixture was cooled to room temperature, centrifuged, and washed with ethanol three times (30 mL ethanol per time). Finally, YSMSNs-NH₂ were obtained under vacuum drying at 50 °C overnight. In addition, to explore the effect of amine content on the catalytic activity, the comparative samples with different volume of amine reagent chemical treatment (1 mL, 2 mL, 4 mL, and 5 mL) were prepared accordingly with the same procedure to the 3 mL APTES grafting on the YSMSNs. Generally, the YSMSNs-NH₂ refers to the product of 3 mL APTES grafting on the YSMSNs except for the particular description.

2.2. Synthesis of Pd/YSMSNs-NH₂(x-y) catalysts

A series of Pd/YSMSNs-NH₂(x-y) catalysts were prepared by a facial wet chemical co-reduction approach using sodium borohydride (NaBH₄) as the reducing agent (x is the Pd loading in the catalysts with a wt% as the unit and y is the amount of amine reagent used for the surface functionalization with a mL as the unit) to explore the effects of Pd loading amount and amine group content of these addressed catalysts for the FA dehydrogenation. Typically, for the synthesis of optimized catalyst Pd/YSMSNs-NH₂(10–3) as an example, putting sodium tetrachloride palladium (15.00 mg, 0.05 mmol, Na₂PdCl₄) and 48.9 mg of YSMSNs-NH₂ into deionized water (5 mL). Following a 30-minute ultrasonic treatment, the mixture was subsequently transferred to an agitator for stirring. Subsequently, an excess of NaBH₄ (37.8 mg, 1 mmol) was introduced into the aforementioned mixture, and stirring continued for an additional 30 min. Once the complete reduction of the metal was achieved, the combined solution was subjected to centrifugation (10000 rpm, 8 min) and washed thrice with copious amounts of deionized water. Finally, the resulting solid was dried under vacuum conditions at 323 K overnight to yield the desired Pd/YSMSNs-NH₂(10–3) catalyst. In addition, to study the effect of Pd loading amount of the resulting catalysts on the catalytic activity, Pd/YSMSNs-NH₂(x-3, x = 5, 10, 15, 20, 25) catalysts were prepared by fixing the APTES grafting at 3 mL. Similarly, to investigate the amine group content of the resulting catalysts on the catalytic activity, Pd/YSMSNs-NH₂(10-y, y = 0, 1, 2, 3, 4, 5) catalysts were synthesized by fixing the Pd loading at 10 wt%. It is worth mentioned that when y is 0, the Pd/YSMSNs-NH₂(10–0) is presented as Pd/YSMSNs in the context for convenience. As exhibited in the Table S1, a series of catalysts are denoted as Pd/YSMSNs-NH₂(x-y) with different Pd loading and amine content.

2.3. Catalyst characterization

The characterization methods of X-ray photoelectron spectroscopy (XPS), powder X-ray Diffraction (XRD), scanning electron microscope (SEM), high-resolution transmission electron microscope (TEM), N₂ adsorption/desorption isotherms, inductively coupled plasma-optical emission spectrometry (ICP-OES), elemental analyses (N, C, and H), Fourier Transform Infrared spectroscopy (FTIR), and gas chromatograph (GC) were provided clearly in SI.

2.4. Catalytic test

The catalytic performance of the catalysts prepared for FA dehydrogenation was assessed by monitoring the rate of gas production. In a two-necked round-bottom flask (20 mL), as depicted in Fig. S1, one of the necks was connected to a gas collection apparatus, while the other was utilized for introducing the FA-SF mixed solution. Specifically, the freshly prepared catalyst was dissolved in 3 mL of deionized water within the two-necked flask. Subsequently, 2 mL of the FA-SF mixture (FA: 2.5 mmol) with a molar ratio of 1:2, unless otherwise specified, was introduced into the reaction system to initiate FA dehydrogenation reactions under vigorous stirring. It is noted that the $n_{\text{Pd}}/n_{\text{FA}}$ molar ratio is 1:50 for the catalytic reactions except for the specific notification. Furthermore, a controlled-temperature oil bath was used to maintain the reaction temperature at the predetermined value, facilitating the initiation of reactions at varying temperatures.

3. Result and discussion

3.1. Fabrication and characterization of the catalyst

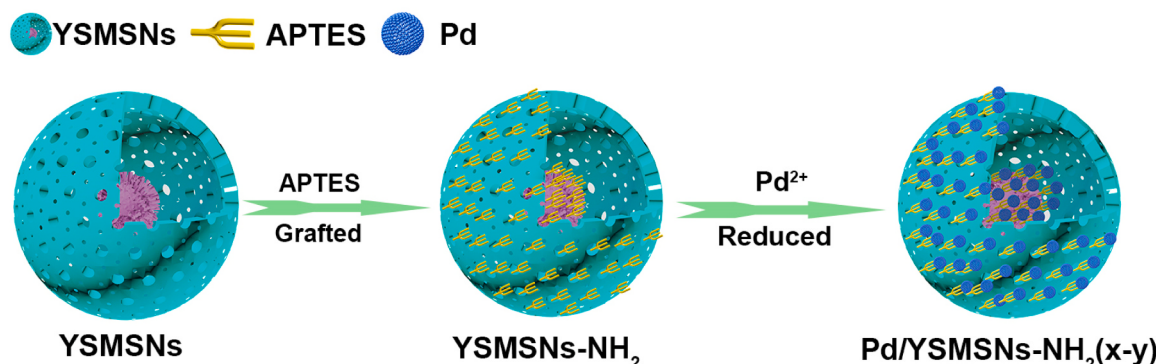
The oriented yolk shell mesoporous channels of YSMSNs are endowed with silanol groups, which lend themselves readily to amine group modifications. This property renders them highly amenable to anchoring active metals during the synthetic procedure. As exhibited in Scheme 1, The surface functionalization of YSMSNs with -NH₂ was adeptly accomplished, and this successful modification was corroborated by the analysis of FTIR spectra (Fig. S2); the presence of grafted -NH₂ groups was readily identifiable at wavenumbers of 686 and 1550 cm⁻¹, which could be ascribed to N-H as γ vibration and δ vibration in amine groups, respectively[40]. These YSMSNs-NH₂ were effectively utilized as a support matrix for the immobilization of Pd NPs.

Upon examination of the wide-angle XRD patterns of both YSMSNs-NH₂ and Pd/YSMSNs-NH₂(10–3) (Fig. 1a), it is evident that both materials display a pronounced broad peak within the 20–30° range, which is the amorphous SiO₂ in the as-prepared samples. Compared to the YSMSNs-NH₂ support, Pd/YSMSNs-NH₂(10–3) displays a characteristic diffraction peak of Pd (111), which indicates the Pd species are introduced to the YSMSNs-NH₂ support successfully. XPS analyses were carried out to scrutinize the chemical states and electronic attributes of Pd/YSMSNs-NH₂ and its comparative counterparts. As depicted in Fig. 1b, discernible signals corresponding to Pd, N, O, and Si were evident for Pd/YSMSNs-NH₂(10–3), thus confirming the successful incorporation of Pd into the YSMSNs-NH₂ support. Subsequently, the N 1 s peak of YSMSNs-NH₂ exhibited two distinctive components centered at 399.3 eV (-NH₂) and 401.5 eV (-NH₃⁺). In contrast, the higher N 1 s peaks at 399.9 eV (-NH₂) and 401.7 eV (-NH₃⁺) were discernible in the case of Pd/YSMSNs-NH₂(10–3), as depicted in Fig. 1c. This observation suggests that the YSMSNs-NH₂ support transfers electrons to the Pd NPs,

thereby establishing an electron-rich surface on the Pd NPs. This phenomenon substantiates the manifestation of MSI between the introduced Pd NPs and the YSMSNs-NH₂ support. Additionally, this MSI effect is also confirmed by the Pd 3d of Pd/YSMSNs-NH₂(10–3) and Pd/YSMSNs (Fig. 1d). It is observed that the peaks of Pd⁰ in the Pd/YSMSNs are located at 336.0 eV (Pd⁰ 3d_{5/2}) and 341.2 eV (Pd⁰ 3d_{3/2}), and the corresponding peaks of Pd/YSMSNs-NH₂(10–3) are shifted to the lower binding energies of 335.7 eV (Pd⁰ 3d_{5/2}) and 340.9 eV (Pd⁰ 3d_{3/2}), respectively. In summary, the YSMSNs-NH₂ support plays a pivotal role as an electron donor, thereby exerting influence over the electronic structure of the resulting Pd NPs through the MSI effect. Consequently, the MSI-induced formation of electron-rich and well-dispersed Pd NPs significantly enhances the efficacy of FA dehydrogenation. It is noteworthy to highlight that a minor presence of Pd²⁺ in both Pd/YSMSNs and Pd/YSMSNs-NH₂(10–3) could account for the partial oxidation of surface Pd⁰ during the XPS study.

The pore structural properties of YSMSNs, YSMSNs-NH₂, and Pd/YSMSNs-NH₂(10–3) are studied by N₂ physisorption. As presented in Fig. 2a, the N₂ adsorption-desorption isotherms reveal that all the prepared samples exhibit two distinct capillary steps in the P/P₀ ranges of 0.1–0.2 and 0.85–0.95, respectively. The results imply that two series of pores coexist in the samples. Furthermore, the N₂ adsorption-desorption isotherms of these samples exhibit a type IV curve with two different hysteresis loops. The first, a substantial H₂ hysteresis loop, is evident in the relative pressure range of 0.45 to 0.9, signifying a narrow mesoporous pore size distribution. The second, an H₃ hysteresis loop, emerges within the relative pressure range of 0.9 to 1.0, indicative of a broader pore size distribution. As exhibited in Fig. 2b, all the as-prepared samples have double mesoporous structure. For the YSMSNs, the small pores and large pores are estimated to be 2.1 nm and 14.8 nm, which is similar to the previous work[52]. After the surface functionalization, for the YSMSNs-NH₂, the corresponding small pores and large pores become 2.5 nm and 14.8 nm. For the Pd/YSMSNs-NH₂(10–3) catalyst, the diameters of the small pores and large pores are measured to be 2.2 nm and 14.5 nm. Compared to the pristine YSMSNs, the distinctive decrease on the specific surface area and pore volume of YSMSNs-NH₂ and Pd/YSMSNs-NH₂(10–3) disclose that amine group and the Pd NPs are introduced to the YSMSNs-NH₂(10–3) successfully (Table S2).

The morphological and pore characteristics of the YSMSNs-NH₂ and Pd/YSMSNs-NH₂(10–3) catalyst were studied by SEM and TEM characterizations. SEM images, as depicted in Fig. 3a for YSMSNs-NH₂ and Fig. 3d for Pd/YSMSNs-NH₂(10–3), confirm the presence of mono-dispersed nanosphere morphology, with an approximate size of 200 nm, closely resembling the morphology of pristine YSMSNs (Fig. S3a-b), which is similar to the previous work[52]. Moreover, the TEM images of Pd/YSMSNs-NH₂(10–3) (Fig. 3e-f) reveal that it retains obvious yolk-shell structure, where a dark yolk is covered with a gray layer and consists of radially oriented mesoporous channels, which is similar to the YSMSNs-NH₂ (Fig. 3b-c) and pure YSMSNs (Fig. S3c-d).



Scheme 1. Schematic representation for the synthetic strategy of the Pd/YSMSNs-NH₂(x-y).

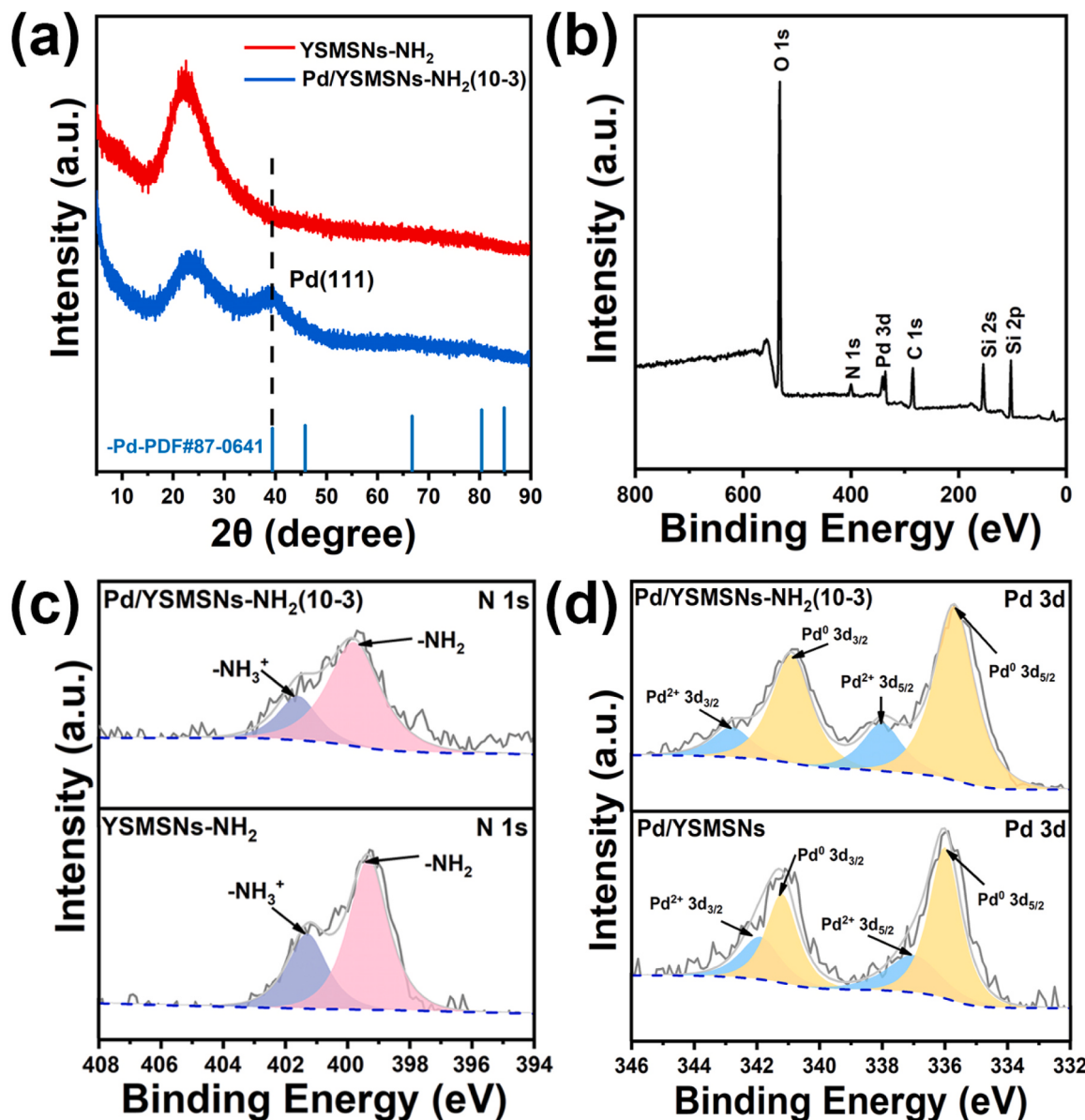


Fig. 1. (a) XRD analyses of YSMSNs-NH₂ and Pd/YSMSNs-NH₂(10-3), (b) XPS full spectrum of Pd/YSMSNs-NH₂(10-3), (c) XPS spectra of N 1 s of Pd/YSMSNs-NH₂(10-3) and YSMSNs-NH₂, (d) XPS spectra of Pd 3d of Pd/YSMSNs-NH₂(10-3) and Pd/YSMSNs.

Furthermore, the YSMSNs-NH₂ support showcases the presence of ultra-small Pd NPs with an average size of 1.5 nm, as illustrated in Fig. 3f. In contrast, the Pd NPs supported on pristine YSMSNs lacking surface modification with amine groups, referred to as Pd/YSMSNs, exhibit notably larger particles with a size of 2.9 nm, as depicted in Fig. 3h, which is about two times of the size of Pd NPs within Pd-YSMSNs-NH₂(10-3). This observation underscores the effective immobilization of Pd NPs and the prevention of NP aggregation to larger entities due to the presence of surface amine groups within the YSMSNs. As illustrated in the Fig. 3g, the EDS elemental mappings of Pd/YSMSNs-NH₂(10-3) manifest the simultaneous and homogeneous distribution of Pd, N, O, and Si elements. This observation serves to further substantiate the presence of Pd NPs within the YSMSNs-NH₂, aligning with the finding from XPS analysis. Furthermore, the HRTEM of Pd/YSMSNs-NH₂(10-3) reveals the lattice spacing of Pd NPs is 0.228 nm (Fig. S4), which is similar to the (111) plane of face-centered cubic (fcc) Pd and is consistent with the wide-angle XRD result. In summary, the ultrafine size and exceptional dispersion of Pd NPs on the YSMSNs-NH₂ platform offer the potential for efficient FA

dehydrogenation by Pd/YSMSNs-NH₂(10-3).

3.2. Activity test of FA dehydrogenation

The examination of the catalytic performance of Pd/YSMSNs-NH₂(x-3) catalysts in the context of FA dehydrogenation was conducted at a temperature of 323 K. Firstly, to investigate the effect of Pd loading amount on the catalytic activity, various Pd loading Pd/YSMSNs-NH₂(x-3) were prepared by fixing the APTES grafting at 3 mL. As displayed in Fig. 4a, in this condition, all the catalysts exhibited the 100% FA conversion. As to the initial TOF, Pd/YSMSNs-NH₂(10-3) emerged as the most proficient in terms of catalytic performance among the various candidates. It exhibited the release of 122 mL of mixed gas within around 3 min. The TOF, calculated based on the total molar quantity of Pd element, reached 2783 h⁻¹, with the initial FA conversion attaining 20%. Moreover, Pd/YSMSNs-NH₂(10-3) displayed the shortest completed reaction time and best initial TOF among the tested Pd/YSMSNs-NH₂(x-3) catalysts with different Pd loading (Table S3). Moreover, it is noteworthy that the TOF stands as one of the highest

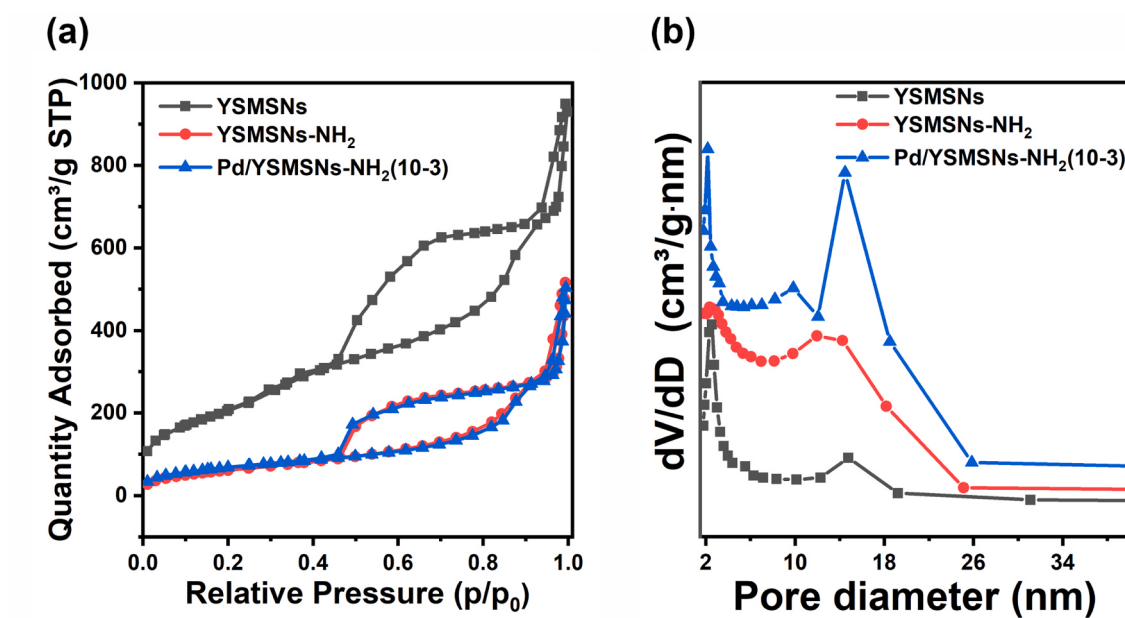


Fig. 2. (a) N_2 adsorption-desorption isotherms of YSMSNs, YSMSNs-NH₂, and Pd/YSMSNs-NH₂(10-3), (b) Pore distribution curves of YSMSNs, YSMSNs-NH₂, and Pd/YSMSNs-NH₂(10-3).

values recorded within the category of monometallic Pd-based heterogeneous systems under comparable catalytic conditions, as evidenced by data available in Table S9 in the SI. Furthermore, the gaseous mixtures resulting from the FA decomposition consist of H₂ and CO₂ in a volumetric ratio of 1:1, without any detectable formation of CO during the course of this process. This was verified through NaOH trap and GC experiments, as illustrated in Fig. S5 and S6, affirming a remarkable 100% H₂ selectivity. It is noted that the catalytic activity started to decrease from Pd loading at 15 wt%, and it should be the agglomeration of Pd NPs and the decrease of Pd dispersion by the increase of metal loading. The incorporation of -NH₂ functional groups onto the YSMSNs-NH₂ confers a positive impact on the catalytic activity of the resultant catalysts. Hence, to elucidate the impact of the amine content within YSMSNs-NH₂ on catalytic activity, various catalysts denoted as Pd/YSMSNs-NH₂(10-y) were prepared while maintaining a fixed Pd loading of 10 wt%. As depicted in Fig. 4b, the Pd NPs supported on unmodified YSMSNs (Pd/YSMSNs) exhibited nearly negligible catalytic activity, as evidenced by the minimal release of gas mixtures during the catalytic process. Particularly, the FA conversion could only achieve 10% in the whole catalytic reaction, with approximately 10 min to reach this point by Pd/YSMSNs, and the corresponding TOF could be 31 h⁻¹ calculated by this FA conversion (10%) and related time. Furthermore, a comprehensive investigation into the influence of the quantity of APTES functionalization on the YSMSNs support revealed a significant role in catalytic activity. The optimal APTES content was determined to be 3 mL, yielding the highest initial TOF at 2783 h⁻¹ and the shortest completion time for the reaction, approximately 3 min, among all the assessed Pd/YSMSNs-NH₂(10-y) catalysts (Table S4). Especially, for the optimized Pd/YSMSNs-NH₂(10-3) and Pd/YSMSNs, the TOF values of normalizing H₂ production rates to the number of surface Pd atoms were also explored. According to the metal dispersion D(%) results of the Pd/YSMSNs-NH₂(10-3) and Pd/YSMSNs (Table S8) and the formula (3) in the SI to calculate TOF_{surface}, the TOF_{surface} values of Pd/YSMSNs-NH₂(10-3) and Pd/YSMSNs were 5547 h⁻¹ and 176 h⁻¹, respectively. As inferred from the experimental findings outlined above, the amine groups present on the YSMSNs can be regarded as Brønsted basic sites, creating a basic environment in the vicinity of the Pd NPs. This environment plays a crucial role in facilitating the dissociation of the O-H bond within FA. Moreover, the varying content of amine groups within YSMSNs-NH₂ can effectively modulate the MSI effect, thereby exerting a

discernible influence on the catalytic performance in FA dehydrogenation. Additionally, the presence of these amine groups contributes to the formation of ultrafine Pd NPs, ensuring their high dispersion and consequently enhancing the overall catalytic efficiency. Through an examination of the content of grafted amine groups onto the YSMSNs-NH₂ support within the resulting catalysts, it becomes apparent that the appropriate treatment with amine reagents assumes a pivotal role in dictating catalytic performance. From the comprehensive studies of effects of Pd loading amount and amine group content about the as-prepared catalysts over FA dehydrogenation, the optimized values of Pd loading and amine group are 10 wt% and 3 mL, respectively. Moreover, to elucidate the influence of the unique radial pores of the YSMSN support over FA dehydrogenation activities, the catalytic activities of the Pd/SBA-15-NH₂ with the conventional porous structure and optimized Pd/YSMSNs-NH₂(10-3) with the radial oriented porous structure were also explored. Obviously, compared to the Pd/SBA-15-NH₂, Pd/YSMSNs-NH₂(10-3) exhibited a better catalytic activity (Fig. S7). The initial TOF of Pd/YSMSNs-NH₂(10-3) is 2783 h⁻¹ at 323 K, and the total reaction time is approximately 3 min. However, under the same catalytic condition, the initial TOF of Pd/SBA-15-NH₂ is 751 h⁻¹, and the corresponding total reaction time is approximately 19 min. Therefore, the improved catalytic activity of Pd/YSMSNs-NH₂(10-3) could be attributed to the radial oriented porous structure for the rapid mass transfer.

Indeed, SF is a carboxylate with alkaline properties, stands as a potent promoter for enhancing the catalytic performance in FA dehydrogenation. Consequently, an investigation was conducted to assess the influence of the molar ratio between FA and SF on FA dehydrogenation employing the optimized Pd/YSMSNs-NH₂(10-3) catalyst. This inquiry determined that the most effective molar ratio of FA to SF is 1:2, yielding an impressive TOF of 2783 h⁻¹. Furthermore, the entire catalytic reaction process can be accomplished around 3 min (Fig. 5), thereby demonstrating the most favorable initial TOF and the shortest duration required to reach completion in comparison to other FA/SF molar ratio systems (Table S5). The findings elucidate that the introduction of SF can significantly enhance the rate of H₂ production. Remarkably, it is noteworthy that even in the absence of SF, the optimized Pd/YSMSNs-NH₂(10-3) catalyst continues to exhibit commendable catalytic activity, yielding a TOF of 1336 h⁻¹ with 100% FA conversion at 323 K. This TOF is notably comparable to that of the most proficient heterogeneous

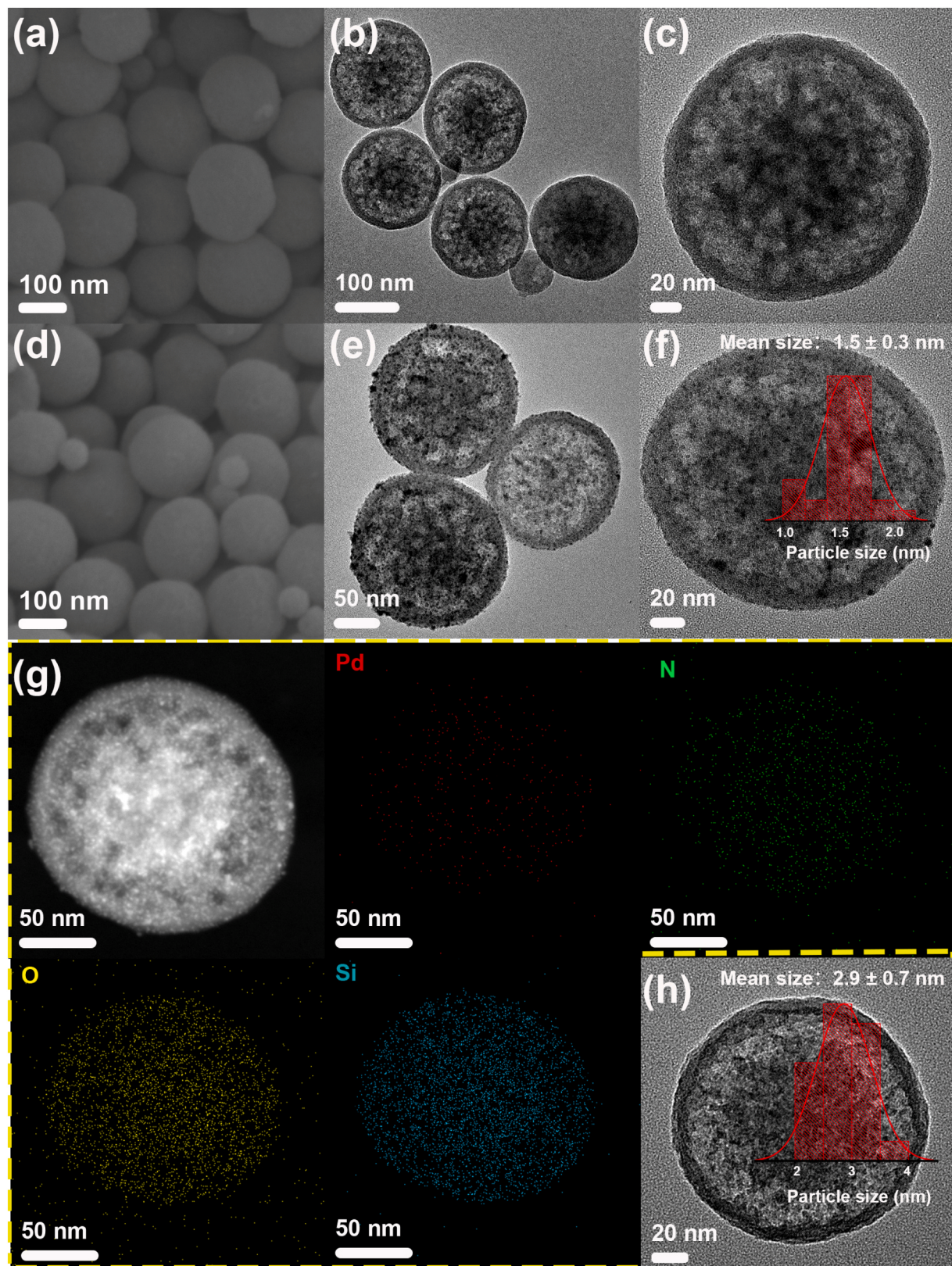


Fig. 3. (a) SEM image of YSMSNs-NH₂, (b-c) TEM images of YSMSNs-NH₂, (d) SEM image of Pd/YSMSNs-NH₂(10–3), (e-f) TEM images of Pd/YSMSNs-NH₂(10–3) (in the f, insert: size distribution of the NPs), (g) EDS mapping of Pd/YSMSNs-NH₂(10–3), (h) TEM of Pd/YSMSNs (insert: size distribution of the NPs).

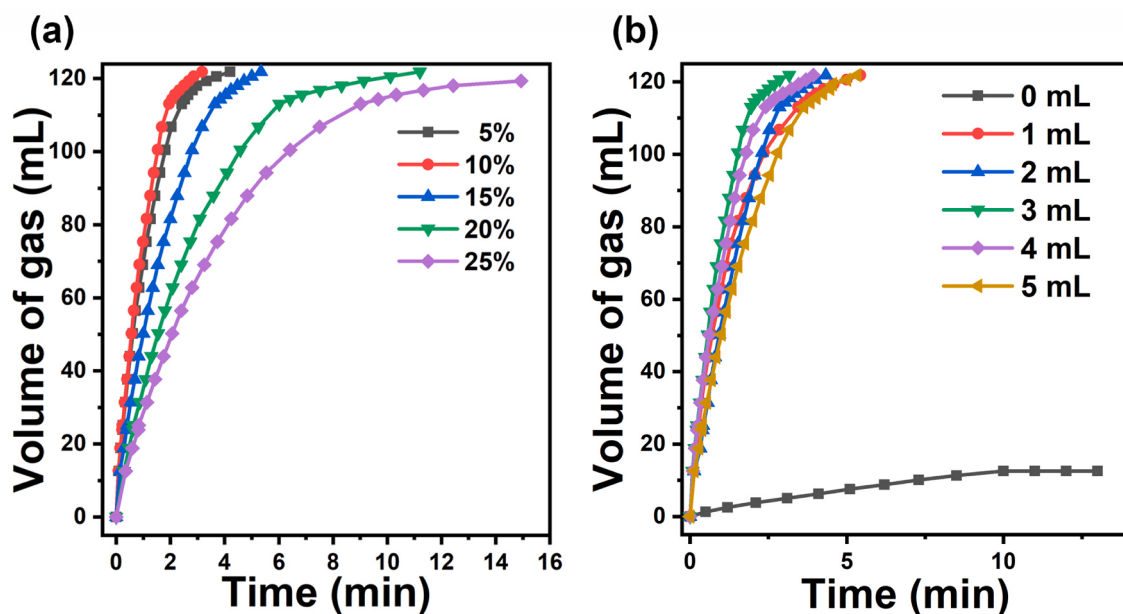


Fig. 4. The volume of released gas versus time for the FA dehydrogenation in the FA/SF mixed solution at 323 K by (a) Pd/YSMSNs-NH₂(x-3) with different Pd loading ($n_{\text{FA}}/n_{\text{SF}} = 1:2$; $n_{\text{metal}}/n_{\text{FA}} = 0.02$) (b) Pd/YSMSNs-NH₂(10-y) with different dosage of APTES ($n_{\text{FA}}/n_{\text{SF}} = 1:2$; $n_{\text{metal}}/n_{\text{FA}} = 0.02$).

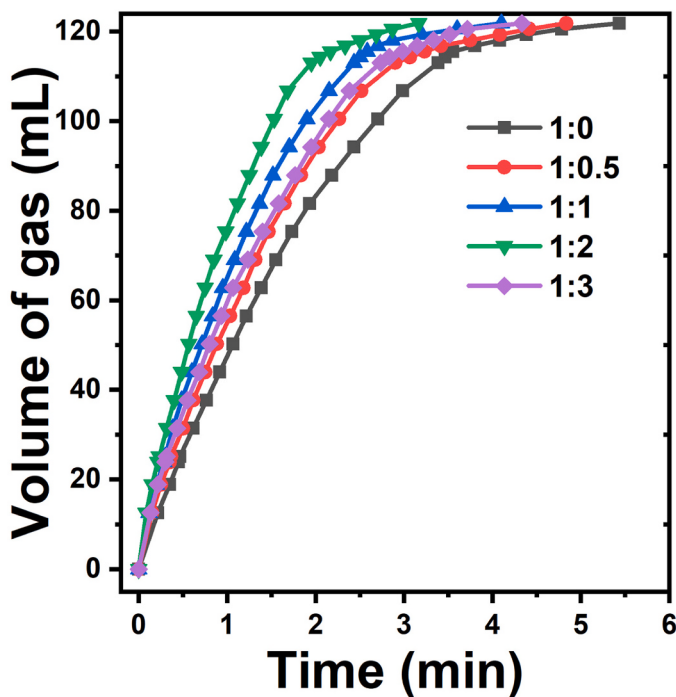


Fig. 5. The volume of released gas versus time by Pd/YSMSNs-NH₂(10-3) for the FA dehydrogenation with different molar ratio of FA/SF at 323 K ($n_{\text{metal}}/n_{\text{FA}} = 0.02$).

catalysts employed in FA dehydrogenation under analogous reaction conditions (Table S9).

Detailed investigations were conducted to unravel the catalytic reaction kinetics of FA dehydrogenation over the Pd/YSMSNs-NH₂(10-3) catalyst. As depicted in Fig. 6a, the catalytic reaction exhibits characteristics closely with a nearly zero-order reaction with respect to FA concentration, as discerned from the initial rate of gas generation (where FA conversion attains 20%). Furthermore, when scrutinizing the initial rate of gas generation, the reaction closely approximates a first-

order reaction concerning catalyst concentration, as revealed in Fig. 6b. Beyond these observations in Fig. 6a-b, the catalytic performance of Pd/YSMSNs-NH₂(10-3) was further examined at varying temperatures. Complying with the Arrhenius equation, the activation energy (E_a) for FA dehydrogenation within the FA-SF mixture was determined to be 39.3 kJ/mol (as illustrated in Fig. 6c). This value notably stands lower than those reported for the majority of heterogeneous Pd-based catalysts in similar reaction conditions (refer to Table S9). Furthermore, Fig. 6d provides an overview of the TOF values, spanning 626, 1207, 2783, 4007, and 9108 h⁻¹, each recorded at distinct reaction temperatures (303, 313, 323, 333, and 343 K).

3.3. Reusability experiment

Reusability assessments of the Pd/YSMSNs-NH₂(10-3) in FA dehydrogenation were conducted at 323 K. As illustrated in Fig. 7a-b, the Pd/YSMSNs-NH₂(10-3) catalyst demonstrated remarkable stability throughout six successive runs, with no discernible alterations in either the initial TOF or total reaction duration per run. Characterization of the recovered catalysts involved several analytical techniques, including XRD, TEM, EA, and ICP-OES. Results confirmed the retention of the crystal structure and Pd content of Pd/YSMSNs-NH₂(10-3), substantiated by XRD (Fig. 7c) and ICP-OES data (Table S6), when comparing the recycled catalyst to the original. TEM imaging (Fig. S8) revealed an increased particle size of 2.2 nm in the recovered Pd/YSMSNs-NH₂(10-3), which may be ascribed to Pd NPs aggregation. Additionally, a partial reduction in the grafted amine groups of Pd/YSMSNs-NH₂(10-3) was evident in the results of EA (Table S6). It can be inferred that the marginally increased particle size and amine group loss contributed to a subtle decline in catalytic activity. In summary, the observations detailed above underscore the commendable reusability of the optimized Pd/YSMSNs-NH₂(10-3) catalyst in FA dehydrogenation.

3.4. Mechanism study

To study the reaction mechanism of FA dehydrogenation over the optimized Pd/YSMSNs-NH₂(10-3) catalyst, studies regarding the kinetic isotope effect (KIE) were systematically conducted. The related KIE experiments were conducted with Pd/YSMSNs-NH₂(10-3) using HCOOH, HCOOD, and DCOOH [54–56]. As exhibited in the Table 1, the

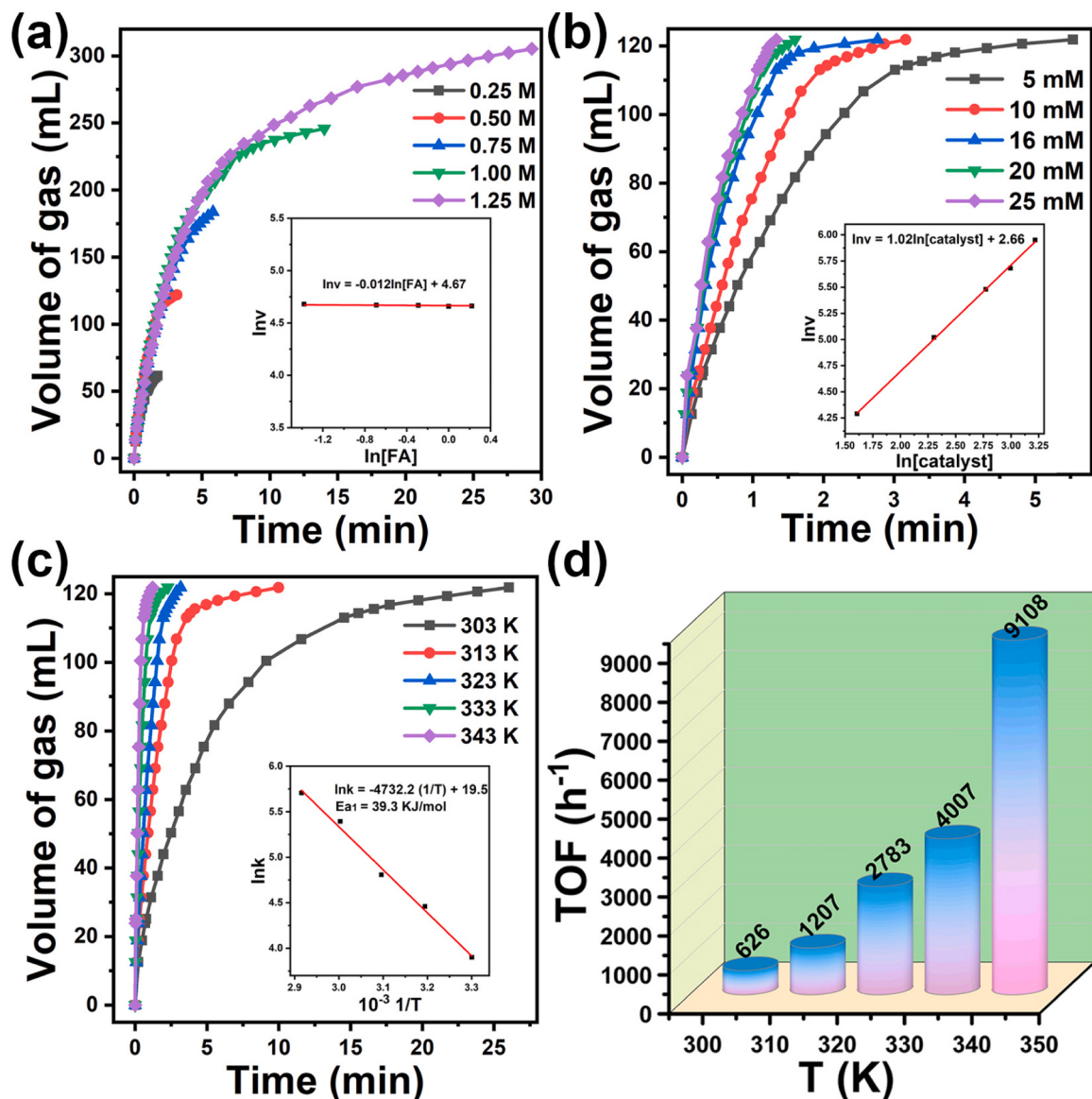


Fig. 6. The volume of released gas versus time by Pd/YSMSNs-NH₂(10-3) for the FA dehydrogenation at varying (a) FA concentrations, (b) catalyst concentration, (c) catalytic reaction temperatures, and (d) related TOF values. Inset: corresponding kinetic parameters.

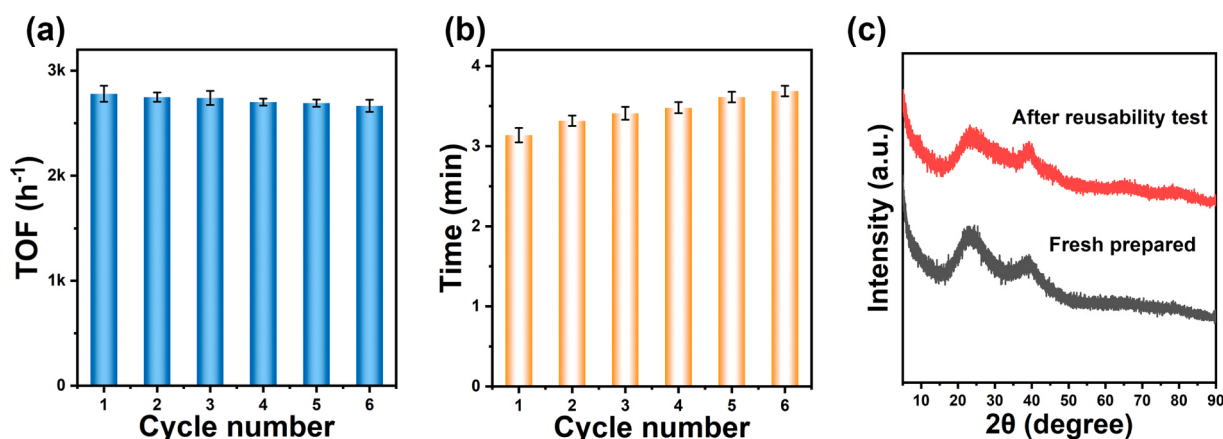


Fig. 7. (a) Initial TOF of Pd/YSMSNs-NH₂(10-3) for FA dehydrogenation in FA-SF aqueous solution at 323 K ($n_{\text{metal}}/n_{\text{FA}} = 0.02$) for the different cycles over the reusability test, (b) total reaction time of Pd/YSMSNs-NH₂(10-3) for FA dehydrogenation in FA-SF aqueous solution at 323 K ($n_{\text{metal}}/n_{\text{FA}} = 0.02$) for the different cycles over the reusability test (b) XRD analyses of Pd/YSMSNs-NH₂(10-3) before and after reusability test.

Table 1KIE in the FA dehydrogenation using Pd/YSMSNs-NH₂(10–3) catalyst^a.

entry	reactant	TOF ^b (h ⁻¹)	KIE
1	HCOOH	2783	
2	HCOOD	2254	1.23
3	DCOOH	934	2.98

^a Reaction conditions: 0.05 mmol Pd element in the catalyst, FA/SF solution (2.5 mmol FA, $n_{FA}/n_{SF} = 1:2$, 5 mL), 323 K; ^bTOF was calculated when the reactant conversion reaches 20%.

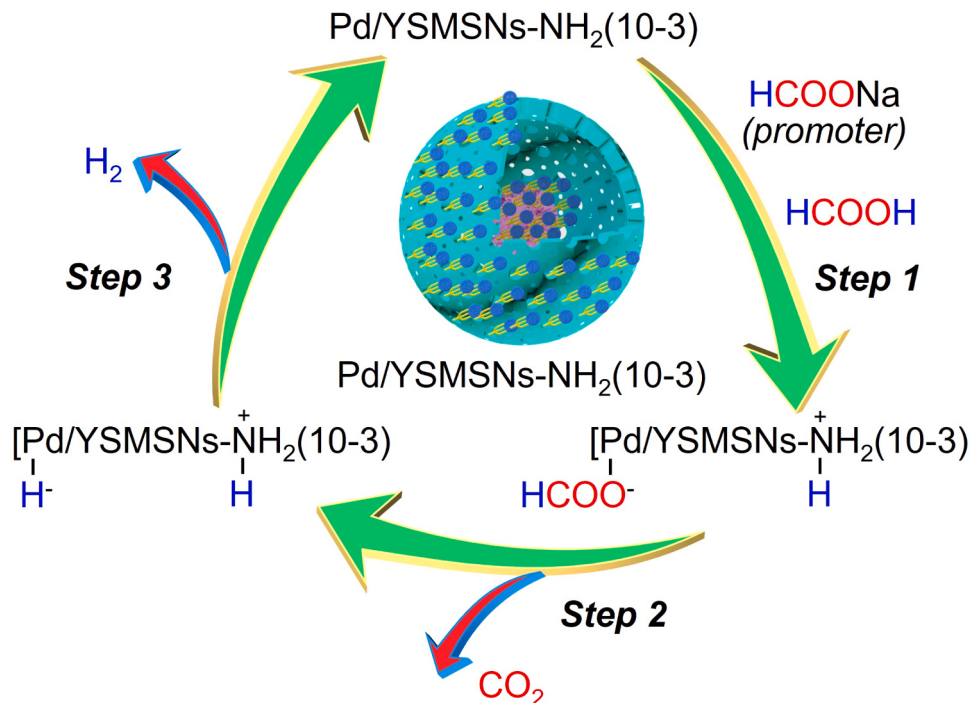
KIE values, which were defined as the reaction rate between the initial TOF (FA conversion reaches 20%) of HCOOH and the initial TOF (deuterated reactant conversion reaches 20%) using the HCOOD and DCOOH. The KIE value was 1.23 when HCOOD was used and 2.98 when DCOOH was employed. The observations provide insights indicating that the rate-determining step (RDS) within the catalytic cycle of FA dehydrogenation involves the cleavage of the C-H bond during the decarboxylation process.

In light of the experimental findings presented earlier and in consideration of previous research on FA dehydrogenation using Pd-based heterogeneous catalysts[40,44,45,57,58], we propose a plausible reaction mechanism for FA dehydrogenation by Pd/YSMSNs-NH₂(10–3), as illustrated in **Scheme 2**. Initially, in the first step, the grafted basic -NH₂ groups on the YSMSNs assist in the dissociation of the O-H bond in FA, resulting in the formation of $-\text{[HNH}_2^+\text{]}$ species and the generation of $[\text{HCOO}]^+$ Pd entities. Subsequently, in the second step, the produced $[\text{HCOO}]^+$ Pd intermediate undergoes C-H bond cleavage to yield $[\text{Pd}[\text{H}]^+]$ species and CO₂, recognized as the RDS in the cycle. Finally, in the third step, the interaction between $-\text{[HNH}_2^+\text{]}$ and $[\text{Pd}[\text{H}]^+]$ gives rise to H₂ production, allowing Pd/YSMSNs-NH₂(10–3) to initiate the next catalytic cycle. Thus, the presence of surface amine groups on the YSMSNs-NH₂, the MSI, and the ultrafine size and high dispersion of Pd NPs collectively contribute to the remarkable catalytic performance observed in FA dehydrogenation.

3.5. Theoretical calculations

To have a better understanding of the excellent catalytic activity of the optimized Pd/YSMSNs-NH₂(10–3) catalyst over FA dehydrogenation, the related theoretical calculations were carried out carefully. Firstly, the diffusions of FA molecules within the conventional silica with uniform porous structure (channel No.1) and YSMSNs with radial oriented porous structure (channel No.2) were explored systematically to reveal the differences of mass transfer in these two types of pore structures. The molecular dynamics (MD) was conducted in Gromacs v5.1.5, and the related snapshots were provided by the Visual Molecular Dynamics software. The detailed simulation methods were similar to the previous works[59,60]. The configurations of simulation systems of initial frame of FA and water in channel No.1 and channel No.2 were displayed **Figure a** and **c**, respectively, with the aqueous solution phases closely matched the experimental details. Additionally, the free volumes in these two channels were approximately equal to have a better understanding of the roles of pore orientations. Furthermore, the dynamical delivery processes of FA molecules in these two channels were also studied, and the different colored FA molecules are randomly selected. As demonstrated in **Fig. 8b** and **d**, compared to the channel No.1, FA molecules could travel longer pathway within channel No.2 over a fixed period time from the snapshots for molecular dynamics in these two channels at different stages. Moreover, to study the difference of the mass transfer in these two channels, the mean square displacement (MSD) was also analyzed. As depicted in **Fig. S9a-b**, the FA exhibited larger MSD values in channel No.2 compared to channel No.1, demonstrating a faster transport rate. Additionally, the diffusion coefficient of FA in channel No.2 is 13.4×10^{-6} cm²/s, more than double that in channel No.1 (5.9×10^{-6} cm²/s). Specifically, the delivery rate along the channel-direction increases by 241% from channel No.1 to channel No.2, rising from 6.3×10^{-6} cm²/s to 21.5×10^{-6} cm²/s (**Fig. S9c**). Thus, the diffusion analysis reveals that the channel No.2 could generate a faster delivery rate of FA molecules. Overall, the unique radial oriented porous structure of YSMSNs could produce a faster mass transfer and improve the FA dehydrogenation activity.

To explore the significance of amine groups of the optimized Pd/



Scheme 2. Proposed reaction mechanism for FA dehydrogenation by Pd/YSMSNs-NH₂(10–3).

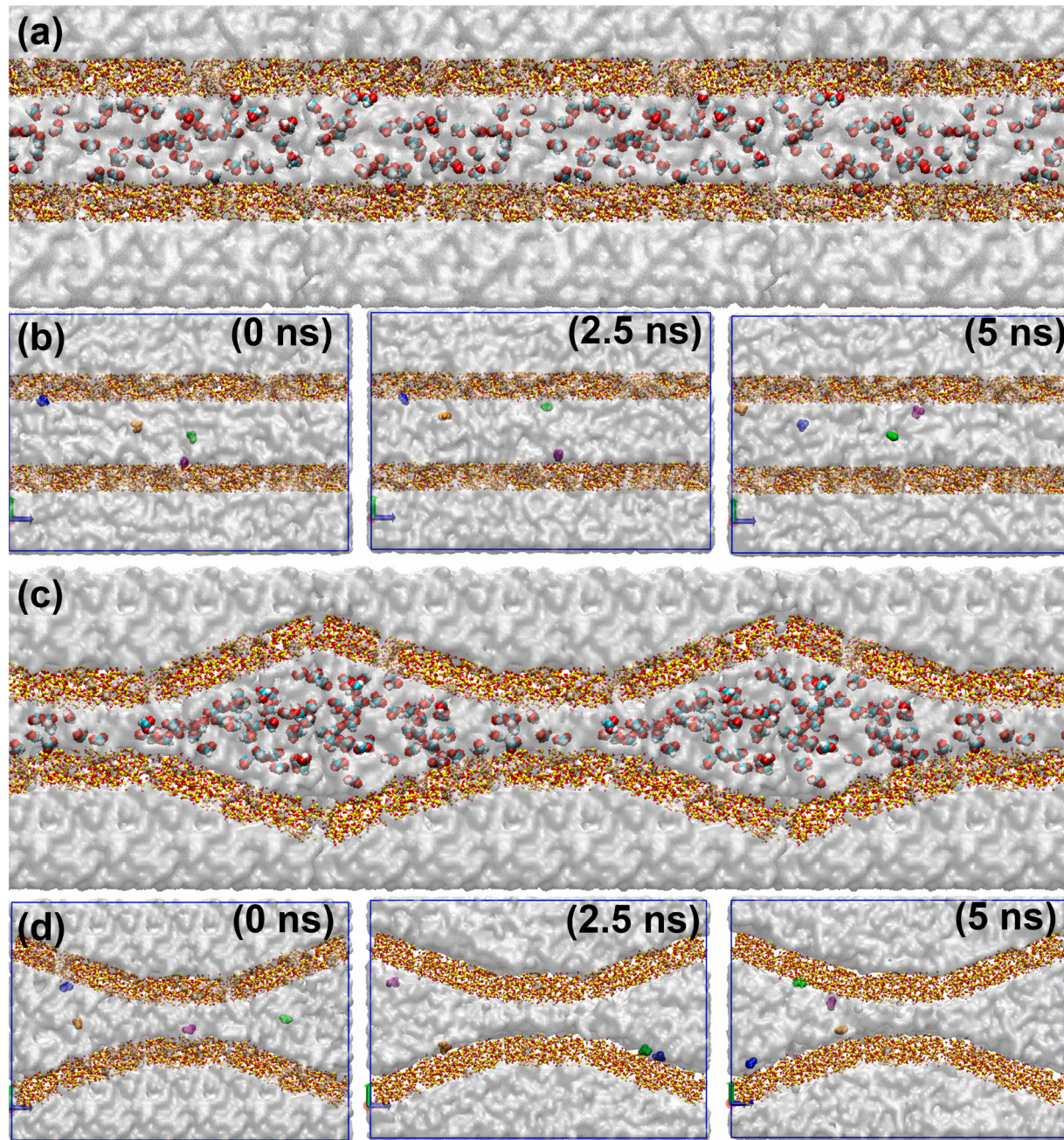


Fig. 8. (a) Configuration of simulation system of initial frame of FA and water in conventional silica with uniform mesoporous structure (channel No.1), (b) related snapshots for molecular dynamics of FA in channel No.1 at different simulation stages, (c) configuration of simulation system of initial frame of FA and water in YSMSNs with radial oriented mesoporous structure (channel No.2), (d) related snapshots for molecular dynamics of FA in channel No.1 at different simulation stages.

YSMSNs-NH₂(10–3) for the improved catalytic performance, the corresponding calculation models were established and investigated by the density functional theory (DFT)[61–66]. As displayed in Figs. 9a and 9c, the charge of Pd clusters in Pd/YSMSNs-NH₂(10–3) is 0.19 e more than that of the Pd/YSMSNs and its geometrical morphology is also more intact, revealing the electron rich Pd active centers in Pd/YSMSNs-NH₂(10–3), further indicating the existence of amine groups benefit for the stabilization of Pd active sites. The results exhibited above are also confirmed by the deformation charge density (DCD) for Pd clusters adsorptions (Figs. 9b and 9d). Fig. 9e shows the potential energy for the dissociation of the O-H bond in FA over the Pd/YSMSNs-NH₂(10–3) and Pd/YSMSNs calculation models, and Fig. 9f exhibits the corresponding initial state (IS), transition state (TS), and final state (FS) configurations. The results clearly reveal that the

required energy for O-H bond dissociation at Pd active sites in Pd/YSMSNs-NH₂(10–3) is 0.36 eV, which is lower than Pd/YSMSNs (0.52 eV), indicating that the amine groups could promote the dissociation process of HCOOH on the Pd clusters. It can be further verified by the carefully observed IS, TS, and FS structures. Although the geometrical morphologies of the sole HCOOH adsorption and the HCOO and H co-adsorption over the Pd/YSMSNs and Pd/YSMSNs-NH₂(10–3) models are almost same, the TS structures are different. Detailly, the H⁺ could occur on the hetero-Pd atoms in the Pd/YSMSNs-NH₂(10–3) models while the H⁺ could only be found on the same Pd atoms in the Pd/YSMSNs. It is because the Pd clusters of the Pd/YSMSNs-NH₂(10–3) demonstrate the electron rich characteristic (Figs. 9b and 9d). Therefore, compared to Pd/YSMSNs system, it is favorable to reach the final state configuration in Pd/YSMSNs-NH₂(10–3) case. All the results

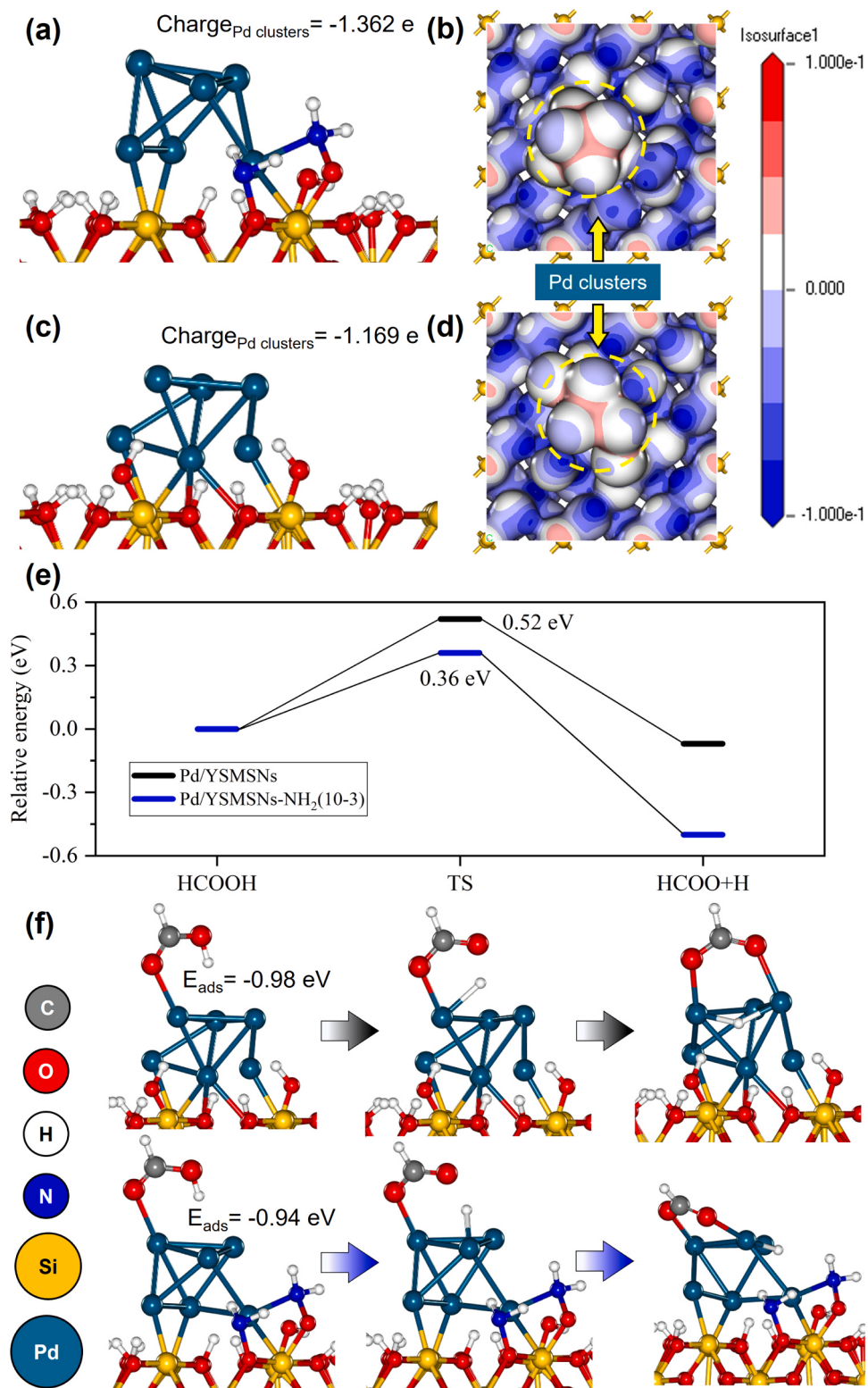


Fig. 9. (a and c) Optimized calculational models for Pd/YSMSNs-NH₂(10-3) and Pd/YSMSNs, (b and d) related deformation charge density (DCD) for Pd clusters adsorptions over Pd/YSMSNs-NH₂(10-3) and Pd/YSMSNs, with the blue and red regions represent the electron loss and the electron accumulation, (e) the relative potential energies of the dissociation of the O-H bond in FA over Pd/YSMSNs and Pd/YSMSNs-NH₂(10-3), (f) the corresponding initial state, transition state, and final state configurations.

exhibited above demonstrate the amine groups could benefit for the formation of the electron rich Pd active site and a favorable environment for the dissociation of the O-H bond in FA towards the enhance catalytic performance.

4. Conclusions

In summary, the Pd/YSMSNs-NH₂(10-3) catalyst exhibits exceptional catalytic proficiency and reusability in the efficient production of

H_2 through FA dehydrogenation. It achieves an impressive initial TOF of 9108 h^{-1} at 343 K, accompanied by 100% FA conversion and H_2 selectivity. Notably, the catalyst maintains its exceptional stability over six consecutive runs, with negligible degradation in catalytic activity. The enhanced FA dehydrogenation observed in Pd/YSMSNs-NH₂(10–3) is attributed to the cooperative interplay of amine groups on the YSMSNs-NH₂ support, the radially oriented pore channels for rapid mass transfer of reactants, the MSI effect, and the fine dispersion of ultrafine Pd NPs. This study presents a facile and effective approach for the development of highly efficient heterogeneous FA dehydrogenation catalysts.

CRediT authorship contribution statement

Wang Xilong: Conceptualization, Data curation, Funding acquisition, Project administration, Resources, Supervision, Validation, Writing – review & editing. **Xu Chunming:** Formal analysis, Resources. **Liu Zhentao:** Data curation, Formal analysis. **Hu Jinsong:** Conceptualization, Formal analysis, Project administration, Resources, Validation, Writing – review & editing. **Duan Aijun:** Formal analysis, Resources. **Yu Ke:** Data curation, Formal analysis. **Liu Quan:** Formal analysis, Methodology, Validation. **Zhou Wenwu:** Formal analysis, Methodology, Validation. **Chai Hao:** Data curation, Formal analysis. **Fan Fei:** Conceptualization, Formal analysis, Methodology, Validation. **Li Song:** Data curation, Formal analysis, Investigation, Methodology. **Zhou Chunhui:** Conceptualization, Data curation, Formal analysis, Funding acquisition, Investigation, Methodology, Project administration, Writing – original draft, Writing – review & editing.

Declaration of Competing Interest

The authors declare that they have no known competing financial interests or personal relationships that could have appeared to influence the work reported in this paper.

Data Availability

Data will be made available on request.

Acknowledgements

This work was financially supported by Scientific Research Foundation for High-level Talents of Anhui University of Science and Technology (2022yzjrc24), the National Natural Science Foundation of China (No. 22308381), Science Foundation of China University of Petroleum-Beijing (No. 2462023QNXZ002) and the National Key R&D Program of China (2021YFA1501201).

Appendix A. Supporting information

Supplementary data associated with this article can be found in the online version at [doi:10.1016/j.apcatb.2024.123750](https://doi.org/10.1016/j.apcatb.2024.123750).

References

- [1] L. Schlapbach, A. Züttel, Hydrogen-storage materials for mobile applications, *Nature* 414 (2001) 353–358.
- [2] A.M. Abdalla, S. Hossain, O.B. Nisfindy, A.T. Azad, M. Dawood, A.K. Azad, Hydrogen production, storage, transportation and key challenges with applications: a review, *Energy Convers. Manag.* 165 (2018) 602–627.
- [3] R. Hren, A. Vujanović, Y. Van Fan, J.J. Klemes, D. Krajnc, L. Čuček, Hydrogen production, storage and transport for renewable energy and chemicals: an environmental footprint assessment, *Renew. Sustain. Energy Rev.* 173 (2023) 113113.
- [4] Q. Yao, Z.-H. Lu, Y. Yang, Y. Chen, X. Chen, H.-L. Jiang, Facile synthesis of graphene-supported Ni-CeO_x nanocomposites as highly efficient catalysts for hydrolytic dehydrogenation of ammonia borane, *Nano Res* 11 (2018) 4412–4422.
- [5] Z.-X. Yang, X.-G. Li, Q.-L. Yao, Z.-H. Lu, N. Zhang, J. Xia, K. Yang, Y.-Q. Wang, K. Zhang, H.-Z. Liu, L.-T. Zhang, H.-J. Lin, Q.-J. Zhou, F. Wang, Z.-M. Yu, J.-M. Ma, Roadmap on hydrogen energy from production to utilizations, *Rare Met* 41 (2022) 3251–3267.
- [6] T. He, Q. Pei, P. Chen, Liquid organic hydrogen carriers, *J. Energy Chem.* 24 (2015) 587–594.
- [7] P.T. Aakko-Saksa, C. Cook, J. Kiviaho, T. Repo, Liquid organic hydrogen carriers for transportation and storing of renewable energy-review and discussion, *J. Power Sources* 396 (2018) 803–823.
- [8] M. Niermann, A. Beckendorff, M. Kaltschmitt, K. Bonhoff, Liquid organic hydrogen carrier (LOHC)-assessment based on chemical and economic properties, *Int. J. Hydrol. Energy* 44 (2019) 6631–6654.
- [9] Y. Sekine, T. Higo, Recent trends on the dehydrogenation catalysis of liquid organic hydrogen carrier (LOHC): a review, *Top. Catal.* 64 (2021) 470–480.
- [10] P. Preuster, C. Papp, P. Wasserscheid, Liquid organic hydrogen carriers (LOHCs): toward a hydrogen-free hydrogen economy, *Acc. Chem. Res.* 50 (2017) 74–85.
- [11] J. Eppinger, K.-W. Huang, Formic acid as a hydrogen energy carrier, *ACS Energy Lett.* 2 (2017) 188–195.
- [12] I. Dutta, S. Chatterjee, H. Cheng, R.K. Parsapur, Z. Liu, Z. Li, E. Ye, H. Kawanami, J. S.C. Low, Z. Lai, X.J. Loh, K.-W. Huang, Formic acid to power towards low-carbon economy, *Adv. Energy Mater.* 12 (2022) 2103799.
- [13] M. Liu, Y. Xu, Y. Meng, L. Wang, H. Wang, Y. Huang, N. Onishi, L. Wang, Z. Fan, Y. Himeda, Heterogeneous catalysis for carbon dioxide mediated hydrogen storage technology based on formic acid, *Adv. Energy Mater.* 12 (2022) 2200817.
- [14] D. Mellmann, P. Sponholz, H. Junge, M. Beller, Formic acid as a hydrogen storage material-development of homogeneous catalysts for selective hydrogen release, *Chem. Soc. Rev.* 45 (2016) 3954–3988.
- [15] S. Chatterjee, I. Dutta, Y. Lum, Z. Lai, K.-W. Huang, Enabling storage and utilization of low-carbon electricity: power to formic acid, *Energy Environ. Sci.* 14 (2021) 1194–1246.
- [16] M. Grasemann, G. Laurenczy, Formic acid as a hydrogen source-recent developments and future trends, *Energy Environ. Sci.* 5 (2012) 8171–8181.
- [17] I. Dutta, R.K. Parsapur, S. Chatterjee, A.M. Hengne, D. Tan, K. Peramaiah, T. I. Solling, O.J. Nielsen, K.-W. Huang, The role of fugitive hydrogen emissions in selecting hydrogen carriers, *ACS Energy Lett.* 8 (2023) 3251–3257.
- [18] Q. Yao, X. Zhang, Z.-H. Lu, Q. Xu, Metal-organic framework-based catalysts for hydrogen production from liquid-phase chemical hydrides, *Coord. Chem. Rev.* 493 (2023) 215302.
- [19] M. Watanabe, T. Sato, H. Inomata, R.L. Smith Jr., Chemical reactions of C1 compounds in near-critical and supercritical water, *Chem. Rev.* 104 (2004) 5803–5822.
- [20] X. Wang, Q. Meng, L. Gao, Z. Jin, J. Ge, C. Liu, W. Xing, Recent progress in hydrogen production from formic acid decomposition, *Int. J. Hydrol. Energy* 43 (2018) 7055–7071.
- [21] C. Guan, Y. Pan, T. Zhang, M.J. Ajitha, K.-W. Huang, An update on formic acid dehydrogenation by homogeneous catalysis, *Chem. Asian J.* 15 (2020) 937–946.
- [22] N. Onishi, R. Kanega, H. Kawanami, Y. Himeda, Recent progress in homogeneous catalytic dehydrogenation of formic acid, *Molecules* 27 (2022) 455.
- [23] J. Li, Q.L. Zhu, Q. Xu, Dehydrogenation of formic acid by heterogeneous catalysts, *Chimia* 69 (2015) 348–352.
- [24] Z. Li, Q. Xu, Metal-nanoparticle-catalyzed hydrogen generation from formic acid, *Acc. Chem. Res.* 50 (2017) 1449–1458.
- [25] Q. Lei, R. Miao, X. Li, X. Liu, Y. Li, Z. He, H. Xie, F. Song, X. Liu, H. Liu, Efficient hydrogen production from formic acid over Ag@AgPd nanotriangulars at room temperature, *Fuel* 355 (2024) 129539.
- [26] M. Karatok, H.T. Ngan, X. Jia, C.R. O'Connor, J.A. Boscoboinik, D.J. Stacchiola, P. Sautet, R.J. Madix, Achieving ultra-high selectivity to hydrogen production from formic acid on Pd-Ag alloys, *J. Am. Chem. Soc.* 145 (2023) 5114–5124.
- [27] P. Poldorn, Y. Wongnongwa, R.-Q. Zhang, S. Nutanong, L. Tao, T. Rungrotmongkol, S. Jungsuttiwong, Mechanistic insights into hydrogen production from formic acid catalyzed by Pd@N-doped graphene: The role of the nitrogen dopant, *Int. J. Hydrol. Energy* 48 (2023) 16341–16357.
- [28] A. Al-Nayili, M. Albdry, AuPd bimetallic nanoparticles supported on reduced graphene oxide nanosheets as catalysts for hydrogen generation from formic acid under ambient temperature, *New J. Chem.* 45 (2021) 10040–10048.
- [29] A.A. Kadhem, A. Al-Nayili, Dehydrogenation of formic acid in liquid phase over Pd nanoparticles supported on reduced graphene oxide sheets, *Catal. Surv. Asia* 25 (2021) 324–333.
- [30] Y. Ding, W. Peng, L. Zhang, J. Xia, G. Feng, Z.-H. Lu, Chromic hydroxide-decorated palladium nanoparticles confined by amine-functionalized mesoporous silica for rapid dehydrogenation of formic acid, *J. Colloid Interface Sci.* 630 (2023) 879–887.
- [31] A. Zhang, J. Xia, Q. Yao, Z.-H. Lu, Pd-WO_x heterostructures immobilized by MOFs-derived carbon cage for formic acid dehydrogenation, *Appl. Catal. B: Environ.* 309 (2022) 121278.
- [32] X. Sun, G. Zhang, Q. Yao, H. Li, G. Feng, Z.-H. Lu, Amine-functionalized carbon bowl-supported Pd-La(OH)₃ for formic acid dehydrogenation, *Inorg. Chem.* 61 (2022) 18102–18111.
- [33] Y.-X. Luo, W. Nie, Y. Ding, Q. Yao, G. Feng, Z.-H. Lu, Robust hydrogen production from additive-free formic acid via mesoporous silica-confined Pd-ZrO₂ nanoparticles at room temperature, *ACS Appl. Energy Mater.* 4 (2021) 4945–4954.
- [34] Z. Zhang, Y. Luo, S. Liu, Q. Yao, S. Qing, Z.-H. Lu, A PdAg-CeO₂ nanocomposite anchored on mesoporous carbon: a highly efficient catalyst for hydrogen production from formic acid at room temperature, *J. Mater. Chem. A* 7 (2019) 21438–21446.
- [35] A. Al-Nayili, H.S. Majdi, T.M. Albayati, N.M.C. Saady, Formic acid dehydrogenation using noble-metal nanoheterogeneous catalysts: towards sustainable hydrogen-based energy, *Catalysts* 12 (2022) 324.

- [36] J. Liang, Z. Liang, R. Zou, Y. Zhao, Heterogeneous catalysis in zeolites, mesoporous silica, and metal-organic frameworks, *Adv. Mater.* 29 (2017) 1701139.
- [37] Y. Zou, C. Xiao, D. Li, A. Wang, D. Gao, H. Shang, C. Wang, A. Duan, C. Xu, X. Wang, Dendritic micro-mesoporous composites via nano-assembly strategy towards high-efficiency catalysts for hydrodesulfurization of dibenzothiophenes, *J. Catal.* 427 (2023) 115092.
- [38] M. Yurderi, A. Bulut, N. Caner, M. Celebi, M. Kaya, M. Zahmakiran, Amine grafted silica supported CrAuPd alloy nanoparticles: superb heterogeneous catalysts for the room temperature dehydrogenation of formic acid, *Chem. Commun.* 51 (2015) 11417–11420.
- [39] L. Wu, B. Ni, R. Chen, C. Shi, P. Sun, T. Chen, Ultrafine PdAu nanoparticles immobilized on amine functionalized carbon black toward fast dehydrogenation of formic acid at room temperature, *Nanoscale Adv.* 1 (2019) 4415–4421.
- [40] Y. Luo, Q. Yang, W. Nie, Q. Yao, Z. Zhang, Z.-H. Lu, Anchoring IrPdAu nanoparticles on NH₂-SBA-15 for fast hydrogen production from formic acid at room temperature, *ACS Appl. Mater. Interfaces* 12 (2020) 8082–8090.
- [41] W. Nie, Y. Luo, Q. Yang, G. Feng, Q. Yao, Z.-H. Lu, An amine-functionalized mesoporous silica-supported PdIr catalyst: boosting room-temperature hydrogen generation from formic acid, *Inorg. Chem. Front.* 7 (2020) 709–717.
- [42] W. Peng, S. Liu, X. Li, G. Feng, J. Xia, Z.-H. Lu, Robust hydrogen production from HCOOH over amino-modified KIT-6-confined PdIr alloy nanoparticles, *Chin. Chem. Lett.* 33 (2022) 1403–1406.
- [43] A. Bulut, M. Yurderi, Y. Karatas, M. Zahmakiran, H. Kivrak, M. Gulcan, M. Kaya, Pd-MnO_x nanoparticles dispersed on amine-grafted silica: highly efficient nanocatalyst for hydrogen production from additive-free dehydrogenation of formic acid under mild conditions, *Appl. Catal. B: Environ.* 164 (2015) 324–333.
- [44] S. Li, C. Zhou, J. Hu, A. Duan, C. Xu, X. Wang, PdIr nanoparticles on NH₂-functionalized dendritic mesoporous silica nanospheres for efficient dehydrogenation of formic acid, *J. Catal.* 426 (2023) 153–161.
- [45] W.-F. Peng, X. Sun, Y. Ding, P. Liu, Q. Yao, Z.-H. Lu, Enhanced activity of WO_x-promoted PdNi nanoclusters confined by amino-modified KIT-6 for dehydrogenation of additive-free formic acid, *ACS Sustain. Chem. Eng.* 11 (2023) 1898–1908.
- [46] J. Wang, Y. Yu, H. Yu, W. Wang, L.-L. Shen, G.-R. Zhang, D. Mei, Covalent triazine framework encapsulated ultrafine PdAu alloy nanoclusters as additive-free catalysts for efficient hydrogen production from formic acid, *ACS Catal.* 13 (2023) 5135–5146.
- [47] K. Koh, J.E. Seo, J.H. Lee, A. Goswami, C.W. Yoon, T. Asefa, Ultrasmall palladium nanoparticles supported on amine-functionalized SBA-15 efficiently catalyze hydrogen evolution from formic acid, *J. Mater. Chem. A* 2 (2014) 20444–20449.
- [48] M.-H. Jin, J.-H. Park, D. Oh, S.-W. Lee, J.-S. Park, K.-Y. Lee, D.-W. Lee, Pd/NH₂-KIE-6 catalysts with exceptional catalytic activity for additive-free formic acid dehydrogenation at room temperature: Controlling Pd nanoparticle size by stirring time and types of Pd precursors, *Int. J. Hydrol. Energy* 43 (2018) 1451–1458.
- [49] S. Zhang, Y. Qian, W.-S. Ahn, Catalytic dehydrogenation of formic acid over palladium nanoparticles immobilized on fibrous mesoporous silica KCC-1, *Chinese J. Catal.* 40 (2019) 1704–1712.
- [50] Z. Teng, S. Wang, X. Su, G. Chen, Y. Liu, Z. Luo, W. Luo, Y. Tang, H. Ju, D. Zhao, G. Lu, Facile synthesis of yolk-shell structured inorganic–organic hybrid spheres with ordered radial mesochannels, *Adv. Mater.* 26 (2014) 3741–3747.
- [51] M. Dang, Z. Teng, X. Su, J. Tao, Q. Hao, X. Ma, Y. Zhang, Y. Li, Y. Tian, J. Zhang, G. Lu, L. Wang, Biphasic-to-monophasic successive Co-assembly approach to yolk-shell structured mesoporous organosilica nanoparticles, *J. Colloid Interface Sci.* 507 (2017) 242–249.
- [52] K. Yu, W. Kong, Z. Zhao, A. Duan, L. Kong, X. Wang, Hydrodesulfurization of dibenzothiophene and 4,6-dimethylbibenzothiophene over NiMo supported on yolk-shell silica catalysts with adjustable shell thickness and yolk size, *J. Catal.* 410 (2022) 128–143.
- [53] K. Yu, W. Kong, Z. Zhao, A. Duan, L. Kong, X. Wang, Hydrodesulfurization over NiMo catalysts supported on yolk-shell silica materials with controllable cavity size, *ChemistrySelect* 7 (2022) e202202376.
- [54] K. Mori, M. Dojo, H. Yamashita, Pd and Pd–Ag nanoparticles within a macroreticular basic resin: an efficient catalyst for hydrogen production from formic acid decomposition, *ACS Catal.* 3 (2013) 1114–1119.
- [55] M. Wen, K. Mori, Y. Kuwahara, H. Yamashita, Plasmonic Au@Pd nanoparticles supported on a basic metal-organic framework: synergic boosting of H₂ production from formic acid, *ACS Energy Lett.* 2 (2017) 1–7.
- [56] M. Navlani-García, D. Salinas-Torres, K. Mori, Y. Kuwahara, H. Yamashita, Enhanced formic acid dehydrogenation by the synergistic alloying effect of PdCo catalysts supported on graphitic carbon nitride, *Int. J. Hydrol. Energy* 44 (2019) 28483–28493.
- [57] F.-Z. Song, Q.-L. Zhu, N. Tsumori, Q. Xu, Diamine-alkalized reduced graphene oxide: immobilization of sub-2 nm palladium nanoparticles and optimization of catalytic activity for dehydrogenation of formic acid, *ACS Catal.* 5 (2015) 5141–5144.
- [58] Q. Liu, X. Yang, Y. Huang, S. Xu, X. Su, X. Pan, J. Xu, A. Wang, C. Liang, X. Wang, T. Zhang, A Schiff base modified gold catalyst for green and efficient H₂ production from formic acid, *Energy Environ. Sci.* 8 (2015) 3204–3207.
- [59] Q. Liu, M. Chen, L. Sun, G. Liu, R. Xu, Pore density effect on separations of water/ethanol and methanol/ethanol through graphene oxide membranes: A theoretical study, *Sep. Purif. Technol.* 308 (2023) 122975.
- [60] Q. Liu, C. Guo, Z. Yang, H. Yao, J. Hu, G. Liu, W. Jin, Enabling efficient water desalination and mitigating membrane fouling by the novel two-dimensional fullerene with unlocking its electrostatic forces, *J. Membr. Sci.* 687 (2023) 122074.
- [61] F. Fan, Z. Chen, A. Zhou, Z. Yang, Y. Zhang, X. He, J. Kang, W. Zhou, Theoretical investigation on the inert pair effect of Ga on both the Ga-Ni-Mo-S nanocluster and the direct desulfurization of 4,6-dimethylbibenzothiophene, *Fuel* 333 (2023) 126351.
- [62] W. Zhou, F. Fan, Z. Chen, A. Zhou, DFT insights into the adsorption behavior of 4,6-dimethylbibenzothiophene on the Ni-Mo-S corner sites: Effect of the promoter magnetism, *Appl. Surf. Sci.* 569 (2021) 150992.
- [63] Y. Xie, J. Wu, G. Jing, H. Zhang, S. Zeng, X. Zou, J. Wen, H. Su, C.-J. Zhong, P. Cui, Structural origin of high catalytic activity for preferential CO oxidation over CuO/CeO₂ nanocatalysts with different shapes, *Appl. Catal. B: Environ.* 239 (2018) 665–676.
- [64] Y. Pan, Y. Chen, K. Wu, Z. Chen, S. Liu, X. Cao, W.-C. Cheong, T. Meng, J. Luo, L. Zheng, C. Liu, D. Wang, Q. Peng, J. Li, C. Chen, Regulating the coordination structure of single-atom Fe-N_xC_y catalytic sites for benzene oxidation, *Nat. Commun.* 10 (2019) 4290.
- [65] J.L. Vincent, P.A. Crozier, Atomic level fluxional behavior and activity of CeO₂-supported Pt catalysts for CO oxidation, *Nat. Commun.* 12 (2021) 5789.
- [66] H. Wang, M.S. Bootharaju, J.H. Kim, Y. Wang, K. Wang, M. Zhao, R. Zhang, J. Xu, T. Hyeon, X. Wang, S. Song, H. Zhang, Synergistic interactions of neighboring platinum and iron atoms enhance reverse water-gas shift reaction performance, *J. Am. Chem. Soc.* 145 (2023) 2264–2270.